INL/RPT-22-68379 Rev:000

Milestone 1.2.10: Steady-state H_2 "roll over" point data for aluminum alloys 1100 and 6061

July 2022

Gregory P. Horne, Jacy K. Conrad, Trishelle M. Copeland-Johnson, Xiaofei Pu, Amey Khanolkar, Joseph R. Wilbanks, and Corey D. Pilgrim

Idaho National Laboratory, Center for Radiation Chemistry Research

Idaho National Laboratory

INL is a U.S. Department of Energy National Laboratory operated by Batelle Energy Alliance, LLC

INL/RPT-22-68379 Rev:000

Milestone 1.2.10: Steady-state H_2 "roll over" point data for aluminum alloys 1100 and 6061

Gregory P. Horne, Jacy K. Conrad, Trishelle M. Copeland-Johnson, Xiaofei Pu, Amey Khanolkar, Joseph R. Wilbanks, and Corey D. Pilgrim
Idaho National Laboratory, Center for Radiation Chemistry Research

July 2022

Idaho National Laboratory
Center for Radiation Chemistry Research
Idaho Falls, Idaho, 83415

http://www.inl.gov

Prepared for the
U.S. Department of Energy
Office of Environmental Management
Under DOE Idaho Operations Office
Contract DE-AC07-05ID14517

Page intentionally left blank

ABSTRACT

Extended (> 50 years) dry storage is being evaluated by the U.S. Department of Energy (DOE) for the disposition of ~ 18 metric tons of aluminum-clad spent nuclear fuel (ASNF). Transition of the current ASNF inventory into dry storage—using the standard DOE canister—necessitates a rigorous, predictive understanding of the long-term physical and chemical factors that may influence the integrity of the proposed storage canister, including radiolytic molecular hydrogen (H_2) generation. Current model predictions employ initial radiolytic yields of H_2, the values of which change as the cladding's H_2-precursor inventory is depleted and H_2 itself becomes progressively more involved in radiolytic and surface dissociation processes. Consequently, the absorbed radiation dose that this steady-state H_2 yield corresponds to is essential for the evaluation and improvement of model predictions. Here, we report our findings on the long-term generation of H_2 from the gamma irradiation ($\leq$ 36 MGy) of corroded AA1100 and AA6061 coupons in helium environments at ambient temperature and 50% added RH. Our findings show that AA1100 systems reached steady-state by ~ 36 MGy, while higher doses were necessary for AA6061 systems. This discrepancy was attributed to the AA6061 coupons developing a thicker corrosion layer that led to the trapping of H_2 and its precursors, and potentially additional chemistries, ultimately delaying the depletion of H_2 precursors and the system's "roll over" point. Further, current model predictions—based on previous AA1100 data—do not show steady-state attainment until above 120 MGy, which is not the case for the AA1100 data collected here. Consequently, the new alloy dependent data presented here are important for the continued improvement of predictive computer models for evaluating the feasibility of extended storage of ASNF in helium backfilled canisters.

Page intentionally left blank

CONTENTS

FIGURES

Page intentionally left blank

ACRONYMS

AA1100	aluminum alloy 1100
AA6061	aluminum alloy 6061
$Al_{(s)}$	aluminum metal
Al···OH	aluminum surface bound hydroxyl group
$Al···OH^-$	aluminum surface bound hydroxide group
$Al···OH_2$	aluminum surface bound water
$Al···O^{\bullet}$	aluminum surface bound oxygen atom
$Al···O^{\bullet-}$	aluminum surface bound oxygen radical
ASNF	aluminum-clad spent nuclear fuel
BSE	backscatter electron
cm^{-1}	per centimeter
CR2	Center for Radiation Chemistry Research
DOE	Department of Energy
E_γ	gamma photon energy
e^-	free electron
e_{aq}^-	hydrated electron
EDS	energy-dispersive X-ray spectroscopy
EMTD	Environmental Management-Technology Development
GC	gas chromatography
Gy min^{-1}	Grays per minute
h^+	electron vacancy hole
H_{aq}^+	hydrated proton
$H^{\bullet}$	hydrogen atom
H^-	hydride
H_2	molecular hydrogen
H_2^+	ionized molecular hydrogen
H_2O	water
H_2O*	water excited state
H_2O_2	hydrogen peroxide
He	helium
kV	kilovolts
INL	Idaho National Laboratory
MeV	mega electron volts

MGy	mega Gray
mm	millimeter
mm^2	millimeter squared
nm	nanometers
O	oxygen atom
$^{\bullet}OH$	hydroxyl radical
OH^-	hydroxide
PVC	polyvinyl chloride
RH	relative humidity
s	seconds
SE	scanning electron
SEM	scanning electron microcopy
TCD	thermal conductivity detector
$\tau_{1/2}$	half-life
°C	degrees Celsius
µL	microliter
µm	micrometer
µmol kg^{-1}	micromoles per kilogram
µW	microwatts

Page intentionally left blank

1. INTRODUCTION

Extended (> 50 years) dry-storage is being evaluated by the U.S. Department of Energy (DOE) for the disposition of ~ 18 metric tons of aluminum-clad spent nuclear fuel (ASNF) [1]. Transition of the current ASNF inventory into dry storage—using the standard DOE canister [2-4]—necessitates a rigorous understanding of the long-term physical and chemical factors that may influence the integrity of the proposed storage canister. The radiolytic formation of molecular hydrogen (H_2) is of particular concern due to the radioactive nature of ASNF. The generation of H_2 can lead to aluminum alloy embrittlement, canister pressurization, and the potential formation of explosive and/or flammable gas mixtures [5-8]. Consequently, the DOE Office of Environmental Management-Technology Development (EMTD) Technical Basis for Extended Dry Storage of Aluminum-Clad Spent Nuclear Fuel has spent several years investigating parameters—such as the extent of corrosion, absorbed gamma dose, gaseous environment (air, nitrogen, argon, and helium), relative humidity (RH), and temperature—that underpin the formation of H_2 from irradiated surrogate cladding materials [9-15]. The data gathered by this initiative has been essential for the development of predictive computer models to support technical considerations and the identification of radiation related challenges for the extended dry storage of ASNF [16-19].

Radiolytically generated H_2 from ASNF arises from a combination of the radiolysis of water molecules (H_2O) adsorbed on the cladding surface [20]:

$$H_2O \rightsquigarrow H_2O^*, {}^{\bullet}OH, H^{\bullet}, e_{aq}^{-}, H_2, H_2O_2, H_{aq}^{+}, \quad (1)$$

$$H_2O^* \rightarrow H_2 + O, \quad (2)$$

$$e_{aq}^{-} + e_{aq}^{-} (+2H_2O) \rightarrow H_2 + 2OH^{-}, \quad (3)$$

$$e_{aq}^{-} + H_{aq}^{+} \rightarrow H^{\bullet}, \quad (4)$$

$$e_{aq}^{-} + H^{\bullet} + H_2O \rightarrow H_2 + OH^{-}, \quad (5)$$

$$H^{\bullet} + H_2O \rightarrow H_2 + {}^{\bullet}OH, \quad (6)$$

$$H^{\bullet} + H^{\bullet} \rightarrow H_2, \quad (7)$$

and the radiolysis of aluminum hydroxide and oxyhydroxide layers generated from corrosion processes [21-23]:

$$Al\cdots OH \rightsquigarrow h^{+} + Al\cdots OH^{-}, \quad (8)$$

$$Al\cdots OH^{-} \rightarrow Al\cdots O^{\bullet -} + H^{\bullet}, \quad (9)$$

$$Al\cdots OH_2 + h^{+} \rightarrow Al\cdots OH^{-} + H_{aq}^{+}. \quad (10)$$

However, current model predictions employ initial radiolytic yields of H_2 [16-19], the values of which change as the cladding's H_2-precursor inventory is depleted and H_2 itself becomes progressively more involved in radiolytic (e.g., **Equations 11-13**) and surface dissociation (**Equations 14** and **15** [24,25]) processes:

$$H_2 \rightsquigarrow H^{\bullet}, H_2^{+}, e^{-}, \quad (11)$$

$$H_2 + Al\text{-}O^{\bullet} \rightarrow Al\text{-}OH + H^{\bullet}, \quad (12)$$

$$H^{\bullet} + Al\text{-}OH \rightarrow Al_{(s)} + H_2O, \quad (13)$$

$$H_2 + Al_{(s)} \rightarrow Al_{(s)} + H^{\bullet} + H^{\bullet} \text{ (}\textit{homolytic}\text{)}, \quad (14)$$

$$H_2 + Al_{(s)} \rightarrow Al_{(s)} + H^{-} + H^{+} \text{ (}\textit{heterolytic}\text{)}, \quad (15)$$

until a steady-state yield is attained. The absorbed radiation dose that this steady-state H_2 yield corresponds to is currently unknown and yet is essential for the evaluation and improvement of model predictions.

To this end, we report our findings on the long-term generation of H_2 from the gamma irradiation (≤ 36 MGy) of corroded AA1100 and AA6061 coupons in He environments at ambient temperature and 50% added relative humidity (RH), as measured by gas chromatography (GC). In addition, a suite of surface characterization techniques were employed to identify differences between the corrosion layers of the AA1100 and AA6061 alloys and how they correlate to steady-state H_2 yield attainment.

2. EXPERIMENTAL METHODS

2.1 Materials

AA1100 and AA6061 coupons (2.5 cm × 0.65 cm × 0.15 cm) were purchased from Metals Samples Company - Alabama Specialty Products, Inc. Acetone (HPLC Plus, ≥ 99.9%) and ethanol (absolute, ≥ 99.8%) were supplied by MilliporeSigma. Helium was purchased in its highest available purity from Norco. Ultra-pure water (18.2 MΩ·cm) was used for all water applications. All AA1100 and AA6061 coupons were cleaned, corroded, and flame-sealed as described previously [10].

2.2 Steady-State Gamma Irradiations

Gamma irradiations were performed using the Idaho National Laboratory (INL) Center for Radiation Chemistry Research (CR2) Foss Therapy Services Cobalt-60 Irradiator. Samples comprised of individually flame-sealed borosilicate glass ampules containing a single corroded AA1100 or AA6061 coupon sealed under a He gaseous environment at 50% added RH—conditions found to promote the greatest H_2 yield for previously reported AA1100 irradiations in nitrogen and argon environments [10]. Samples were loaded into a multi-position sample holder and irradiated at ambient irradiator temperature (~ 45 °C, as determined using a calibrated NI USB-TC01 Single Channel Temperature Input Device equipped with a K-type thermocouple) over several months to achieve the desired radiation dose. Chemical dosimetry was used to determine each sample position's dose rate (Gy min^{-1}) using Fricke solution [26]. Measured dose rates were subsequently corrected for the decay of cobalt-60 ($\tau_{1/2}$ = 5.27 years; $E_{\gamma 1}$ = 1.17 MeV and $E_{\gamma 2}$ = 1.33 MeV) and aluminum metal electron density (0.8673) [27].

2.3 Quantification of Headspace Molecular Hydrogen

Gas chromatography—using a Shimadzu Co. (Kyoto, Japan) Nexus GC-2030 gas chromatograph equipped with a benchmarked TCD set at 200 °C—was used to quantify the amount of H_2 in the headspace of each flame-sealed vial. GC settings were as previously used [10]. Sampling used a crush-tube method, wherein the flame-sealed sample ampules were cracked inside a length of tubing (Nalgene, 8005 braided PVC) that was fitted with a septum on one end [14]. The headspace of the tubing was then sampled in 100 µL aliquots with a gas-tight syringe (Hamilton, Model 1810 RN) and injected into the GC. All headspace injections were repeated in triplicate and the results were averaged. The ampule and tubing headspace volumes were determined by filling with water and weighing before and after cracking the ampules. The ideal gas law—employing calculated gas yields, the measured headspace volumes for the tubing and the ampule, and the known pressure of He at which the ampule was sealed—was used iteratively to determine the H_2 pressure in the tubing head-space. This method has an estimated error of ≤ 10% and limits of detection of 0.01-1% H_2 at the 95% confidence level [14]. Quality control checks were performed daily to confirm known concentrations of H_2 relative to measured calibration curves. Initial and steady-state radiolytic yields—*G*-values—of H_2 are reported in µmol kg^{-1} of aluminum coupon, including the base metal and corrosion layer.

2.4 Surface Characterization

Surface characterization techniques were employed to identify differences between the corrosion layers of the AA1100 and AA6061 alloys. The surface roughness of non-corroded AA1100 and AA6061 coupons was measured using a Keyence (Keyence Corporation, Osaka, Japan) VK-X250 laser scanning confocal microscope. Surface topography was obtained over multiple 85 µm × 85 µm regions by focusing

the laser beam with a 150× microscope objective lens. The average surface roughness was calculated from the surface topography within 15 µm × 15 µm regions between surface relief features introduced by polishing.

Scanning electron microscopy (SEM) of the surface was used to characterize sample morphology and examine the extent of surface corrosion into the bulk specimen by using cross-section cuts. Specimens were characterized using a JEOL (Peabody, Massachusetts, USA) JSM 6610 LV equipped with an EDAX (Pleasanton, California, USA) Apollo X energy-dispersive X-ray spectroscopy (EDS) detector (10 mm^2 active area). Secondary electron (SE) and backscatter electron (BSE) images were captured at an accelerating voltage of 15 kV, and a working distance of ~ 10 mm.

Raman spectroscopy was used to characterize the localized distribution of surface hydroxide and oxyhydroxide corrosion species initially detected by SEM analysis. Raman spectra were collected in ambient laboratory conditions using a LabRAM (HORIBA Jobin Yvon SAS, Edison, New Jersey, USA) HR confocal microscope equipped with a long focal length (800 mm) Czerny-Turner type spectrograph. A 532 nm continuous wave laser beam emitted by a Coherent Verdi laser was used for excitation of Raman-active modes. The laser beam was passed through a confocal pinhole of 400 µm diameter, and a motorized slit set to a width of 100 µm, and finally focused at normal incidence on the sample surface to a ~ 2 µm diameter spot using a 50× objective lens. The power of the laser beam incident on the sample was ~ 450 µW. Raman spectra were acquired with an exposure time of 20 seconds and over 2 accumulations in the 20-4000 cm^{-1} range. For each sample, measurements were performed on multiple locations.

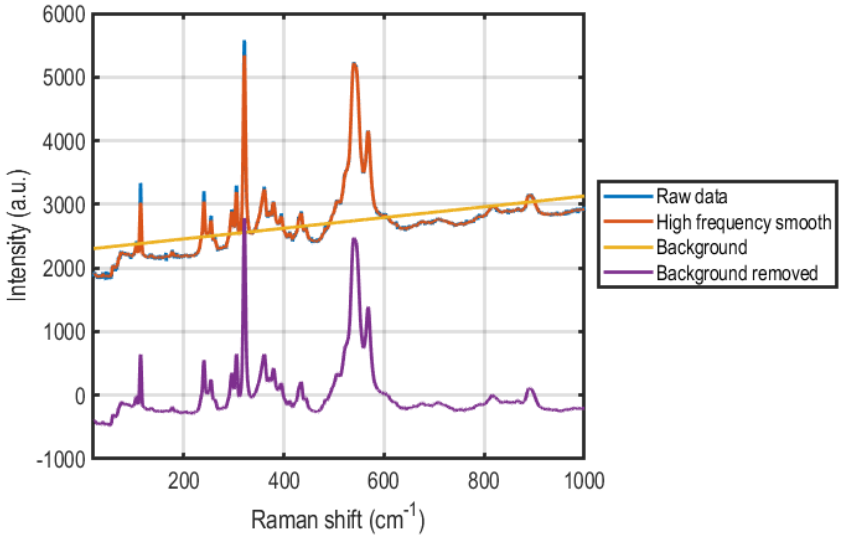

Figure 1. Signal processing procedure applied to a raw Raman spectrum acquired in the 20-1000 cm^{-1} wavenumber range on a corroded AA6061 coupon that received a gamma irradiation dose of 0.66 MGy.

Signal processing, analysis, and visualization of the Raman spectra was performed using a user-defined routine in *MATLAB* (MathWorks Inc., Natick, Massachusetts, USA), typical results for which are shown in **Figure 1**. Raman standards used for identification of the corrosion species were obtained through the RRUFFTM database [28] and those reported in the existing literature [29,30].

3. RESULTS AND DISCUSSION

The radiolytic formation of H_2 is shown in **Figure 2** for the gamma irradiation of corroded AA1100 and AA6061 metal coupons in He environments with 50% added RH**.**

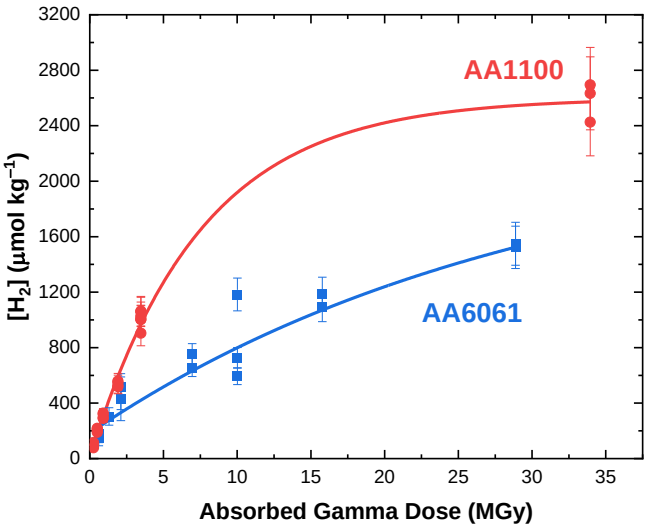

Figure 2. Concentration of H_2 (µmol kg^{-1}) as a function of absorbed gamma dose from the irradiation of corroded AA1100 (●) and AA6061 (■) coupons in He environments at ambient irradiator temperature (~ 45 °C) and 50% added RH. Solid curves are exponential fits to data to guide the eye.

Both aluminum alloys exhibited linear formation of H_2 up to ~ 4 MGy, after which, there is a distinct decrease in the rate of H_2 formation as a steady-state is approached or attained. In agreement with our previous aluminum alloy comparison study [14], the corroded AA1100 samples afforded a greater radiolytic yield of H_2 throughout the investigated dose range in comparison to the corroded AA6061 samples for ~ 50% RH.

Concerning the corroded AA1100 samples, a steady-state H_2 yield of $(2.58 \pm 0.26) \times 10^{-3}$ µmol kg^{-1} was reached by ~ 34 MGy, as indicated by the plateaued exponential fit shown in **Figure 2**. To confirm this observation, several higher dose (40, 50, and 60 MGy) irradiations are underway. With regards to the corroded AA6061 sample data shown in **Figure 2**, a steady-state was approached by ~ 30 MGy, affording a H_2 yield of $(1.54 \pm 0.15) \times 10^{-3}$ µmol kg^{-1}. However, the system did not completely plateau indicating a higher dose was necessary to reach a true steady-state. This variance in steady-state attainment is likely due to differences in the corrosion layer thickness and composition between the two alloys. Consequently, surface characterization techniques were employed to elucidate this discrepancy.

SEM micrographs of the non-corroded coupon surfaces are shown in **Figure 3 (A)** and **(B)** for AA1100 and AA6061, respectively. Both samples were somewhat smooth and featureless, aside from residual scratches from the polishing process prior to exposure. The surface roughness—measured using optical micrography and surface topology measurements shown in **Figure 4**—for a non-corroded AA1100 coupon was determined to be 0.43 ± 0.110 µm {**Figure 4 (A)** and **(C)**}, while that of a AA6061 coupon was 0.14 ± 0.037 µm {**Figure 4 (B)** and **(D)**}. The rougher surface of the non-corroded AA1100 coupons, seen in the form of textured features in **Figure 3 (A)** and **Figure 4 (A)** can be attributed to the lower hardness of AA1100 when compared to that of AA6061 [31]. Surface roughness is known to influence the amount of adsorbed water in metals [32]. The relatively higher surface roughness of the non-corroded AA1100 coupons offers more surface area for water absorption, and thus potentially a greater inventory of H_2-precursors compared to AA6061, thereby providing an explanation for the greater yield of H_2 for AA1100 compared to AA6061 in **Figure 2**.

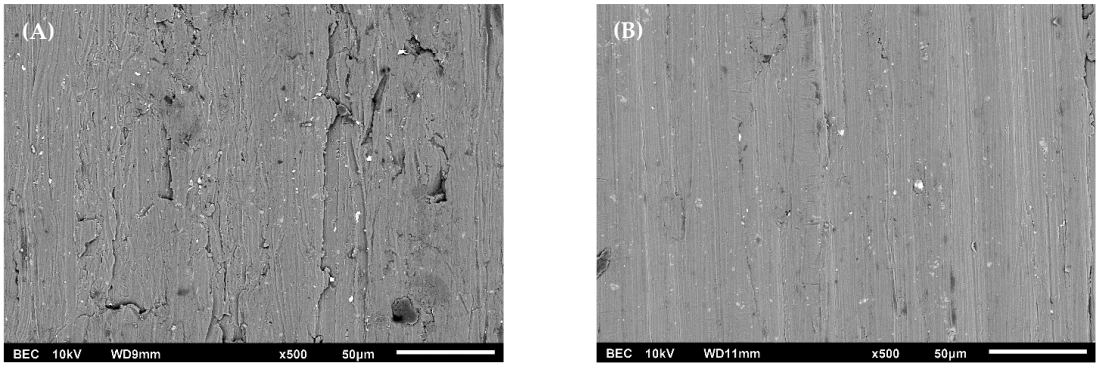

Figure 3. Backscatter electron composition SEM micrograph of the top surface of an as-received coupon of AA1100 **(A)** and AA6061 **(B)**, with scale bars of 50 µm.

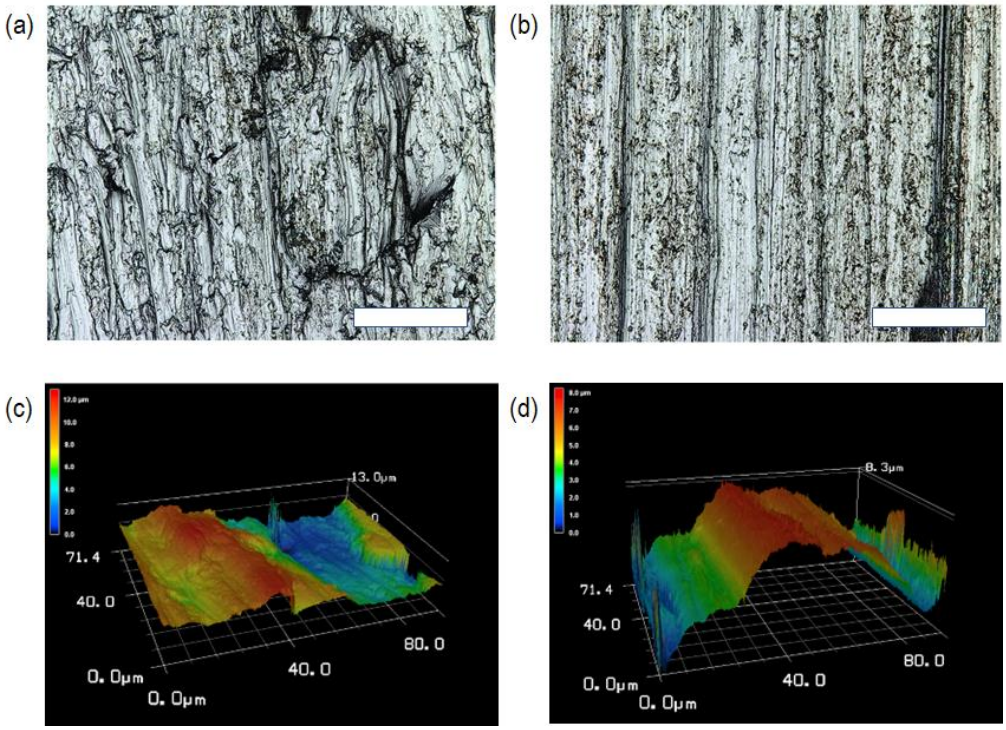

Figure 4. Optical micrographs of non-corroded AA1100 **(A)** and AA6061 **(B)** coupons (scale bars represent 20 µm). Representative surface topography maps for non-corroded AA1100 and AA6061 coupons are shown in panels **(C)** and **(D)**, respectively.

Corrosion of both alloys resulted in a net weight gain from the formation of hydroxide and oxyhydroxide layers. The AA1100 coupons gained an average of 1.45 ± 0.16 mg, whereas the AA6061 coupons gained an average of 4.97 ± 0.70 mg. These results suggest that there was > 3× more corrosion on the AA6061 coupons than the AA1100 samples. The additional corrosion on the AA6061 coupons provides additional sources of H_2-precurors, but also sites for H_2 and its precursors to become trapped and potentially subject to additional chemistries, ultimately delaying the depletion of H_2 precursors and the system's "roll over" point. This may explain why the AA6061 system in **Figure 2** did not reach steady-state within the dose range investigate by this work.

Raman spectroscopy was used to identify the composition of the respective corrosion layers, based on examinations of multiple ~ 2 µm diameter regions per sample. The aluminum oxide/oxyhydroxide mineral phases were identified by comparing peaks in the measured Raman spectra to corresponding peaks in the Raman spectra of alumina phase powders reported previously [28-30], for which typical data is shown in **Figure 5** for a corroded, non-irradiated AA1100 coupon.

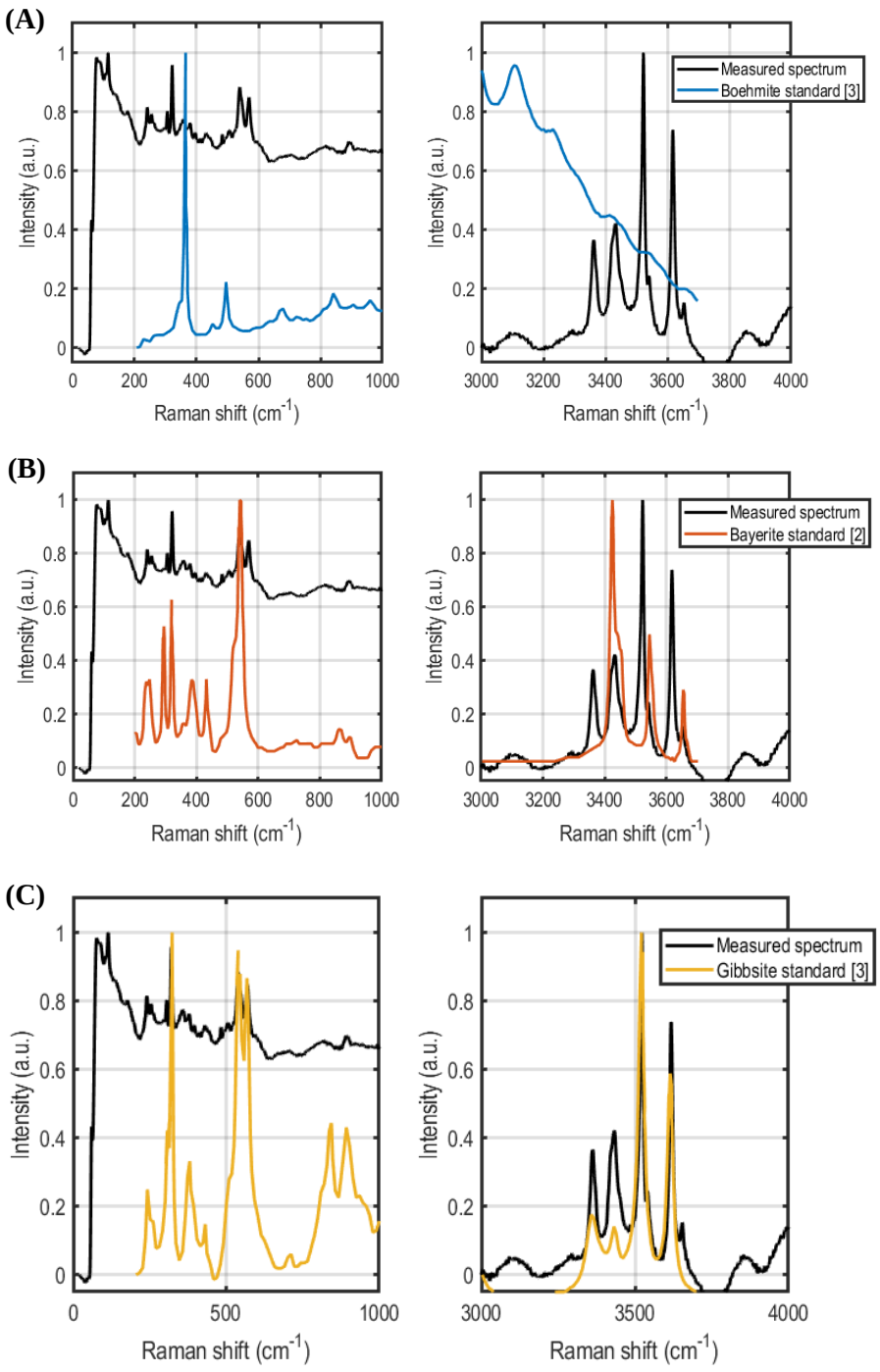
(A)
Intensity (a.u.)
Raman shift (cm-1)
Measured spectrum
Boehmite standard [3]
(B)
Intensity (a.u.)
Raman shift (cm-1)
Measured spectrum
Bayerite standard [2]
(C)
Intensity (a.u.)
Raman shift (cm-1)
Measured spectrum
Gibbsite standard [3]

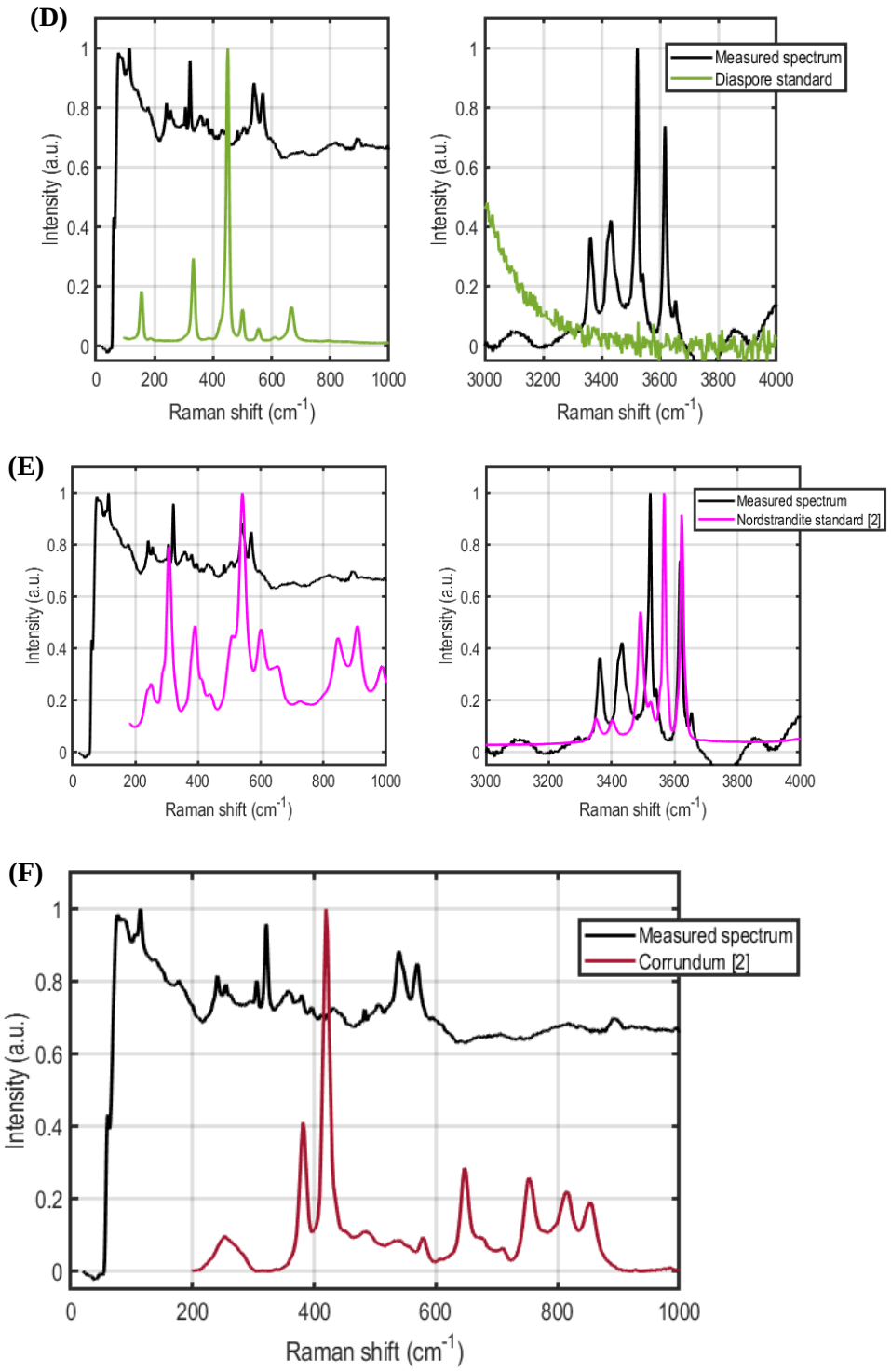

Figure 5. Comparison of the measured Raman spectra for a corroded, non-irradiated AA1100 coupon (**black curve**) with Raman spectra reported for: (**A**) boehmite, (**B**) bayerite; **(C)** gibbsite; **(D)** diaspore powder; **(E)** nordstrandite; and **(F)** corundum standards. [2] = B. Lafuente, R.T. Downs, H. Yang, and N. Stoner, The power of databases: the RRUFF project. In Highlights in Mineralogical Crystallography, T. Armbruster and R.M. Danisi (Eds.); W. De Gruyter, Berlin, Germany, **2015**. [3] = P. Huestis, C.I. Pearce, X. Zhang, A.T. N'Diaye, K.M. Rosso, and J.A. LaVerne, *J. Nucl. Mat.*, **2018**, *501*, 224.

Multiple peaks were observed in the low wavenumber range from 200-1000 cm^{-1} (corresponding to deformation modes of the hydroxyl group), as well as in the high wavenumber region between 3000-4000

cm^{-1} (corresponding to the stretching regime of the hydroxyl group) [30]. Analysis of the measured Raman spectra revealed that bayerite (β-$Al(OH)_3$) was the phase most definitively observed as it was seen for all corroded samples of both alloys, alongside peaks consistent with nordstrandite (γ-$Al(OH)_3$). Some peaks consistent with the presence of gibbsite (α-$Al(OH)_3$) and boehmite (α-AlO(OH)) were observed in most of the corroded samples, and peaks consistent with corundum (Al_2O_3) were observed in a few samples, primarily in the AA1100 coupons. The presence of multiple peaks associated with bayerite and nordstrandite in the measured Raman spectra suggests that these phases reside primarily at the surface. Fewer peaks associated with gibbsite and boehmite were observed in the Raman spectra, suggesting that these species are buried beneath the crystalline surface layer. Raman spectroscopy showed a heterogenous distribution of corrosion products across each sample's surface.

4. CONCLUSIONS

The purpose of this investigation was to determine when a steady-state "roll over" point for radiolytic H_2 production is attained for the gamma irradiation of corroded AA1100 and AA6061 coupons in environments anticipated for the extended long-term storage of ASNF, i.e., in He backfilled atmospheres. Irradiations showed that AA1100 systems reached steady-state by ~ 36 MGy, while higher doses were necessary for AA6061 systems. This discrepancy was attributed to the AA6061 coupons developing a thicker corrosion layer that led to the trapping of H_2 and its precursors, and potentially additional chemistries, ultimately delaying the depletion of H_2 precursors and the system's "roll over" point.

The dose range investigated by this work (≤ 36 MGy) is approximately a third of that anticipated for the full time frame, fuel decay corrected dose range calculated by complimentary dry storage predictive models, i.e., ~ 120 MGy [17]. Based on similar calculations, it was concluded that the amount of H_2 generated within this dose range did not compromise the DOE standard canister's pressure limits [18]. However, current calculations—based on previous AA1100 data—do not show steady-state attainment until above 120 MGy, which is not the case for the AA1100 data collected here. Consequently, the new alloy dependent data presented here are important for the continued improvement of predictive computer models for evaluating the feasibility of extended storage of ASNF in He backfilled canisters

5. ACKNOWLEDGMENTS

This work was supported by the U.S. Department of Environmental Management, Office of Technology Development, under contract DE-AC07-05ID14517.

6. REFERENCES

(1) The Department of Energy Spent Fuel Database (SFD), Version 8.0.7, **2021**.

(2) United States Department of Energy, Preliminary Design, Specification for Department of Energy Standardized Spent Nuclear Fuel Canisters. Idaho Falls, Vol I Design Specification, **1998a**.

(3) United States Department of Energy, Preliminary Design, Specification for Department of Energy Standardized Spent Nuclear Fuel Canisters. Idaho Falls, Vol II Rationale document, **1998b**.

(4) ECAR 4632, Spencer Snow, Supplemental Evaluation of the DOE Standard SNF Canister for Accidental Drops, **2019**.

(5) R. Ambat and E.S. Dwaarakadasa, Effect of hydrogen in aluminium and aluminium alloys: a review. *Bull. Mater. Sci.*, **1996**, *19*, 103.

(6) R.P. Gangloff and B.P. Somerday, Gaseous Hydrogen Embrittlement of Materials. In Energy Technologies, Volume 1 – the Problem, its Characterization and Effects on Particular Alloy Classes. Eds., Elsevier, New York, USA, **2012**.

(7) G. Lu and E. Kaxiras, Hydrogen embrittlement of aluminum: the crucial role of vacancies. *Phys. Rev. Lett.*, **2005**, *94*, 155501.

(8) B. Bonin, M. Colin, and A. Dutfoy, Pressure building during the early states of gas production in a radioactive waste repository. *J. Nucl. Mater.*, **2000**, *281*, 1.

(9) Elizabeth H. Parker-Quaife, Gregory P. Horne, Colt R. Heathman, Peter R. Zalupski, Radiation-Induced Changes in Corrosion of AA1100. INL/EXT-19-52738, Revision 1, **2019**.

(10) E.H. Parker-Quaife, C. Verst, C.R. Heathman, P.Z. Zalupski, and G.P. Horne, Radiation-Induced Molecular Hydrogen Gas Generation in the Presence of Aluminum Alloy 1100. *Rad. Phys. Chem.*, **2020**, *177*, 109117.

(11) G.P. Horne, E.H. Parker-Quaife, C.G. Verst, C.L. Crawford, and R.L. Sindelar, Milestone 2.6: Complete Round-Robin Hydrogen Gas Analysis Capability Comparison. NL/EXT-20-00810, Revision 1, **2020**.

(12) G.P. Horne and E.H. Parker-Quaife, Milestone 2.7: Evaluation of Techniques for the Measurement of Molecular Hydrogen Gas in Helium Matrices. INL/EXT-20-60008, Revision, **2020**.

(13) E.H. Parker-Quaife and G.P Horne, Milestone 2.8: Preliminary Radiolytic Gas Generation Measurements from Helium-Backfilled Samples. INL/EXT-21-61404, Revision 0, **2020**.

(14) G.P. Horne, J.K. Conrad, T.M. Copeland-Johnson, A. Khanolkar, C.D. Pilgrim, J.R. Wilbanks, C. Rae, and E.H. Parker-Quaife, Milestone 1.2.9: Radiolytic Gas Generation Measurements from Helium-Backfilled Samples of AA1100 and AA6061 Coupons. LRS/EXT-21-01823, Revision 0, **2021**.

(15) E. Eidelpes, J. Jarrell, G.P. Horne, J.K. Conrad, C.D. Pilgrim, A.W. Abboud, P. L. Winston, and R. Sindelar, Technical Basis for Extended Dry Storage of Aluminum-clad Spent Nuclear Fuel. *Journal of Nuclear Materials*, **2022**, submitted.

(16) A. Abboud, Modeling Summary of ASNF in DOE Sealed Standard Canisters. INL EXT-21-64413, Revision 0, **2021**.

(17) A. Abboud, Modeling of Radiolytic Hydrogen Generation of Irradiated Surrogate Aluminum Plates. INL-RPT-21-66504 Revision 0, **2021**.

(18) A. Abboud, Extended Modeling of DOE Sealed Canisters with Updated Chemistry Models. INL-RPT-22-67694, Revision 0, **2022**.

(19) A.W. Abboud, Sensitivity study of coupled chemical-CFD simulations for analyzing aluminum-clad spent nuclear fuel storage in sealed canisters. *Nuclear Engineering and Design*, **2022**, *390*, 111691.

(20) G.V. Buxton, C.L. Greenstock, W.P. Helman, and A.B. Ross, Critical review of rate constants for reactions of hydrated electrons, hydrogen atoms and hydroxyl radicals ($^{\bullet}OH/^{\bullet}O^{-}$) in aqueous solution. *J. Phys. Chem. Ref. Data*, **1988**, *17*, 513.

(21) B.H. Milosavljevic and J.K. Thomas, Reactions of Electrons on the Surface of γ-Al_2O_3. A Pulse Radiolytic Study with 0.4 MeV Electrons. *J. Phys, Chem. B*, **2003**, *107*, 11907.

(22) J.K. Thomas, Physical Aspects of Radiation-Induced Processes on SiO_2, γ-Al_2O_3, Zeolites, and Clays. *Chem. Rev.*, **2005**, *105*, 1683.

(23) S. Le Caer, Water Radiolysis: Influence of Oxide Surfaces on H_2 Production under Ionizing Radiation. *Water*, **2011**, *3*, 235.

(24) J. Joubert, A. Salameh, V. Krakoviack, F. Delbecq, P. Sautet, C. Coperet, and J.M. Basset, Heterolytic Splitting of H_2 and CH_4 on y-Alumina as a Structural Probe for Defect Sites. *J. Phys. Chem. B*, **2006**, *110*, 23944.

(25) M. Garcia-Melchor and N. Lopez, Homolytic Products from Heterolytic Paths in H_2 Dissociation on Metal Oxides: The Example of CeO_2. *J. Phys. Chem. C*, **2014**, *118*, 10921.

(26) H. Fricke and E.J. Hart, The Oxidation of Fe^{2+} to Fe^{3+} by the Irradiation with *X*-Rays of Solutions of Ferrous Sulfate in Sulfuric Acid. *J. Chem. Phys.*, **1935**, *3*, 60.

(27) J.W.T. Spinks and R.J. Woods, An Introduction to Radiation Chemistry, Third Edition, Spinks J.W.T.; Woods, R.J. Eds.; Wiley-Interscience, New York, USA, **1990**.

(28) B. Lafuente, R.T. Downs, H. Yang, and N. Stone, The power of databases: the RRUFF project. In Highlights in Mineralogical Crystallography, T. Armbruster and R.M. Danisi (Eds.); W. De Gruyter, Berlin, Germany, **2015**, 1.

(29) Z. Wang, E.D. Walter, M. Sassi, X. Zhang, H. Zhang, X.S. Li, Y. Chen, W. Cui, A. Tuladhar, Z. Chase, A.D. Winkelman, H.-F. Wang, C.I. Pearce, S.B.Clark, and K.M. Rosso, The Role of Surface Hydroxyls on the Radiolysis of Gibbsite and Boehmite Nanoplatelets, *J. Hazard Mater.*, **2020**, *398*, 122853.

(30) H.D. Ruan, R.L. Frost, and J.T. Kloprogge, Comparison of Raman spectra in characterizing gibbsite, bayerite, diaspore and boehmite. *Journal of Raman Spectroscopy*, **2001**, *32 (9)*, 745.

(31) J.F. Shackelford and W. Alexander, CRC materials science and engineering handbook. CRC press, **2000**.

(32) N.D.A. Manaf, K. Fukuda, Z.A. Subhi, and MFM. Radzi, Influences of surface roughness on the water adsorption on austenitic stainless steel. *Tribology International*, **2019**, *136*, 75.